SHORT-WAVELENGTH INFRARED WINDOWS FOR BIOMEDICAL APPLICATIONS

Laura A. Sordillo
Peter P. Sordillo
Editors

SPIE PRESS
Bellingham, Washington USA

Library of Congress Cataloging-in-Publication Data

Sordillo, Laura A., editor. | Sordillo, Peter P., editor.
Title: Short-wavelength infrared optical windows for biomedical applications / Laura A. Sordillo and Peter P. Sordillo.
Description: Bellingham, Washington, USA : SPIE–The International Society for Optical Engineering, [2022] | Includes bibliographical references and index.
Identifiers: LCCN 2021039236 | ISBN 9781510646230 (hardcover) | ISBN 9781510646247 (pdf)
Subjects: LCSH: Biomedical materials. | Artificial intelligence.
Classification: LCC R857.M3 S53 2021 | DDC 610.28–dc23/eng/20211007
LC record available at https://lccn.loc.gov/2021039236

Published by
SPIE
P.O. Box 10
Bellingham, Washington 98227-0010 USA
Phone: +1 360.676.3290
Fax: +1 360.647.1445
Email: books@spie.org
Web: www.spie.org

Cover design by Laura A. Sordillo

Printed in the United States of America.
First printing
For updates to this book, visit http://spie.org and type “PM336” in the search field.

Contents

Preface

One of the most exciting, recent developments in photonics, particularly in regard to its use in medicine and disease, is the utilization of light at wavelengths beyond the visible range and the slightly longer range of short-wavelength infrared (SWIR) wavelengths at 1100–1350 nm, now known as the second optical window. Once ignored because of a lack of sensitive detectors, a third (at 1600–1870 nm) and a fourth (at 2100–2350 nm) optical window are now being utilized extensively. These wavelengths are situated at areas between water peak maxima (where absorption of light is reduced). Due to minimal absorption and scattering of light at these wavelengths, the use of these SWIR optical windows can provide less blurring, better-contrast images, and deeper penetration into tissue media compared with visible light.

With the use of these windows, extensive progress has been made in the study of diseases such as cancer, heart failure, neurocognitive disorders, and diseases of the bone, eyes, skin and teeth. In Part I of this book, investigators review new and emerging techniques based on SWIR light, including the fabrication and use of SWIR nanoparticles as luminescent nanothermometers and photothermal agents, and recent advances in the design, structure and SWIR-related biomedical applications of rare-earth doped nanoparticles (REDNs). REDNs are among the most exceptionally bright and biocompatible SWIR emitters. SWIR imaging techniques—including SWIR hyperspectral imaging for biomedical applications, and a novel wideband (VIS+SWIR) digital holographic microscopic method, based on a novel quantum-dot (QD) image sensor—are also discussed.

In Part II of this book, we explore biomedical applications that employ the SWIR optical windows for the assessment and detection of cancer. SWIR fluorescence and Monte Carlo modeling of breast cancer tissues can reveal important information on how SWIR light interacts with complex media. Recent advances in the study of urothelial carcinoma, a cancer that recurs frequently, are reviewed. SWIR light with multimodal microscopy can be utilized as a minimally invasive diagnostic technique for evaluation of this cancer. Investigators also show how SWIR light can be coupled with fluorescence endoscopy for tumor imaging, and how the assessment of gastrointestinal stromal tumors during surgery can be made using SWIR hyperspectral imaging.

In Part III of this book, we discuss biomedical applications of SWIR light in important diseases of the heart, brain, skin, and other organs. SWIR light can be utilized in the assessment of heart failure and to access difficult-to-reach areas of the brain. Investigators use SWIR imaging techniques to evaluate neurocognitive disorders and skin inflammation. SWIR light can also be employed using an otoscope to assess pediatric conditions, and with optical coherence tomography and other imaging modalities in dentistry.

Finally, Part IV provides a discussion of how artificial intelligence and machine learning can greatly enhance our ability to use SWIR windows to detect and study disease.

Acknowledgments

We would like to thank Ms. Dara Burrows, SPIE Press Senior Editor, for her invaluable help in preparing this book. We would also particularly like to acknowledge Ms. Diana C. Sordillo, M.S., who not only co-authored a chapter, but also made valuable notes and recommendations throughout the book. Finally, we would also like to thank Mr. Vincent T. Sordillo for his technical help, and especially Mrs. Ellen R. Sordillo, M.P.A., for her support.

Laura A. Sordillo, M.S., M.Phil., Ph.D.
Peter P. Sordillo, M.D., Ph.D., M.S.
December 2021

Laura A. Sordillo, M.S., M.Phil., Ph.D. is an interdisciplinary researcher in optics and biophotonics whose work focuses on the discovery of novel short-wavelength infrared techniques for deep tissue imaging of the brain, bone and breast cancer, the use of spectroscopy for the assessment of neurodegenerative diseases such as Parkinson's and Alzheimer's, as well as of cancer, and the study of quantum effects in the brain and in photosynthetic systems. She is currently investigating the application of photonics to quantum computing. She is Director of Biophotonics at Allosteric Bioscience, Inc. and is a research assistant professor at The Institute for Ultrafast Spectroscopy and Lasers in the physics and electrical engineering departments at The City College of New York. She is the recipient of the Kaylie Entrepreneur Award, the MSKCC-CCNY Graduate Research Award, the 2016–2017 Grove School of Engineering Graduate Fellowship, the 2017–2018 Corning Inc. Ph.D. Fellowship Award, and the 2018–2019 Corning Inc. Ph.D. Fellowship Award. She has published more than 60 papers, holds 13 patents, and is coeditor (along with Dr. Peter P. Sordillo M.D., Ph.D., M.S.) of the recently published book *Biophotonics, Tryptophan and Disease* from Elsevier/Academic Press.

Peter P. Sordillo, M.D., Ph.D., M.S. is a physician and cancer researcher whose specialty is the treatment of extremely rare cancers. In addition to his M.D., he holds three graduate degrees in philosophy (causality) (Columbia University), and a graduate degree in physics (New York University). He is Vice-President and Chief Scientific Officer at SignPath Pharma Inc., a biotechnology company; Attending Physician in Medical Oncology, Hematology and Internal Medicine at Lenox Hill Hospital in New York City; and research consultant at The Institute for Ultrafast Spectroscopy and Lasers, Physics Department, The City College of the City University of New York, USA. He has published more than 190 papers, holds 15 patents, and is coeditor (along with Laura A. Sordillo, M.S., M.Phil., Ph.D.) of the recently published book *Biophotonics, Tryptophan and Disease* from Elsevier/ Academic Press.

Chapter 1
Optical Properties of Tissues Using SWIR Light

Francisco J. Salgado-Remacha, Sebastián Jarabo, and Ana Sánchez-Cano
Universidad de Zaragoza, Zaragoza, Spain

performed using this device. The purpose of the first experiment (experiment I) was to validate our system and show how efficient and feasible the supercontinuum (SC)–SWIR system is at measuring the spectral attenuation from 1100–2240 nm from brain and retina tissue. Finally, we calculate the absorption and scattering coefficients in the SWIR range between 1100 and 2300 nm, which are based exclusively on experimental measurements.

1.2 Optical Properties of Major Tissue Components

Biological tissues are heterogeneous materials that contain, e.g., cells and their organelles, protein fibers, DNA, or lipids, and are surrounded by tissue fluids, such as the cytoplasm and interstitial fluid. The attenuation of light in tissue increases at wavelengths corresponding to the absorption bands of the tissue components, while strong light scattering is created by refractive index changes between the tissue component interfaces. The primary absorption bands for the tissue components in the visible (VIS) through the SWIR light range are shown in Fig. 1.1.[24] Key bands are located at 970, 1180, 1450, 1775, 1930, and 1975 nm (due to water); at approximately 760, 830, 920, 1040, 1210, 1430, 1730, 1760, and 1900–2600 nm (lipids); at 420 and 550 nm [deoxygenated hemoglobin (Hb)]; and at 410, 540, and 575 nm [oxygenated hemoglobin (HbO_2)].[10,24,25] In the ultraviolet (UV) range, the primary absorption bands from common tissue components are observed at 200 and 230 nm (proteins); at 260 nm (DNA and RNA); at 275 and 345 nm (HbO_2); and at 275 and 360 nm (Hb).

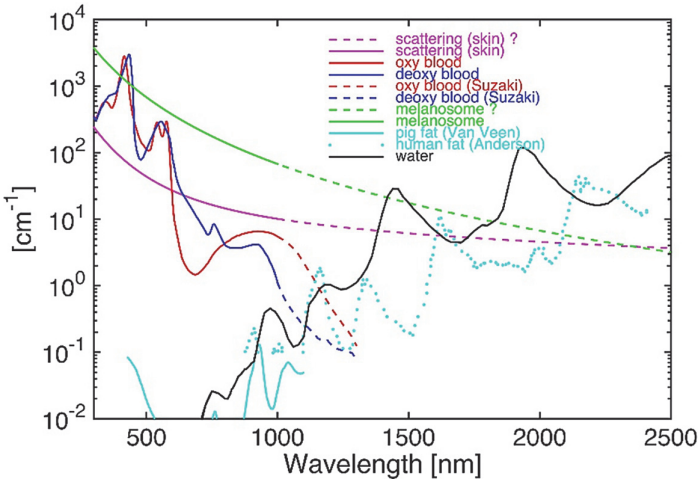

Figure 1.1 Spectral absorption coefficients of some tissue components (water, melanin, fat, HbO_2, and Hb) in the VIS and SWIR regions. Question marks in the key indicate estimated plots. (Reprinted from Ref. 24.)

experimental results obtained in the following sections utilize the fiber collimator system shown in Fig. 1.5(a).

1.5 Spectral Attenuation Measurements of Brain and Retinal Tissues in the SWIR Region: Experiment I

In this section, we measured the spectral attenuation of biological tissues using a SWIR-based SC device and double GRIN-lens filter (as described in the previous section). The spectral attenuation coefficients were measured between 1100 and 2250 nm for two different types of tissues (brain and retina), using the fiber collimator system shown in Fig. 1.5(a). By comparing the signal attenuation versus the tissue depth at different wavelengths, we demonstrate quantitatively the optimum wavelength range for deep brain and retina SWIR imaging.

1.5.1 Materials and methods

Rats used in the experiments were obtained from Dr. M. LaVail (University of California, San Francisco, California, USA) and were bred in a colony at the University of Zaragoza, Zaragoza, Spain. Animals were housed and handled with the authorization and supervision of the Institutional Animal Care and Use Committee from the University of Zaragoza. Procedures were performed in accordance with the ARVO Statement for the Use of Animals in Ophthalmic and Vision Research. Two six-month-old Long–Evans normal rats were injected with a mixture of ketamine (41.7 mg/kg) and xylazine (2.5 mg/kg). The depth of anesthesia was verified using tail and toe pinch reflexes of the lower extremities, and the animals were sacrificed by administering a lethal dose of pentobarbital. The brain and retina were removed, fixed in 4% w/v paraformaldehyde for 1 hour at room temperature, washed in phosphate buffer (pH 7.4 and osmolarity 300 mOsm/kg), and sequentially cryoprotected in 15% w/v sucrose for 1 hour and 30% w/v sucrose overnight at 4 °C. The tissues were sliced at different thicknesses (from 15–100 μm) using a cryostat (Leica Biosystems Nussloch GmbH, Nussloch, Germany).

The ballistic photons (direct transmitted light) were collected using a fiber collimator system. Light transmission spectra were obtained using a custom-made spectroscopic system. A complete description of the laser system can be found in Section 1.3 and in Refs. 34 and 38–40 (Fig. 1.4). The SWIR power was generated from 1100–2250 nm in a highly nonlinear silica fiber, NL-1550-Zero type (Yangtze Optical Fibre and Cable Joint Stock Company Ltd., Wuhan, Hubei, China) pumped with a periodic train of ultrashort pulses. The nominal dispersion of this nonlinear fiber at 1550 nm is null with a dispersion slope of less than 0.025 $ps \cdot nm^{-2} \cdot km^{-1}$. The nonlinear coefficient is greater than 10 $W^{-1} \cdot km^{-1}$, and the Raman gain coefficient is greater than

emission with the use of optical fiber collimators [Fig. 1.5(a)]. With these optical tools, the system can filter efficiently scattered light, leading to an accurate measurement of attenuation values. Spectral attenuation from 1100–2240 nm was measured for both rat brain and retinal tissues. The absorption mechanism has only a small effect on the attenuation coefficient, while the scattering coefficient decreases at longer wavelengths in the SWIR region. This strongly suggest that longer wavelengths in the SWIR range can improve the performance of biophotonic devices by minimizing the spectral attenuation and allowing for deeper penetration into tissue. This also shows that our SC–SWIR system can be used directly on *ex vivo* tissues without the use of optical clearing, with potential clinical applications. Additionally, because diseased tissues commonly have different optical properties compared to healthy tissues, the proposed SWIR technique could be utilized to distinguish healthy and diseased tissues. In the next section, we extend the applications of our SC–SWIR system to rat brain tissue of various thicknesses and a custom-made IR spectrophotometer system.

1.6 Measurement of Optical Properties of *ex vivo* Brain Tissues in the SWIR Range: Experiment II

In experiment I, we were able to validate our SC–SWIR experimental system using brain and retina tissue samples. In experiment II, we performed a deeper analysis on the optical coefficients of biological tissues using two distinct setups: the SC–SWIR system and a custom-made IR spectrophotometer (to measure transmittance from 1100–2300 nm). While absorption is due to the presence of chromophores in tissue, scattering is produced by discontinuities in the refractive index at the microscopic level.[55] Scattering at short wavelengths (primarily from 400–1300 nm) limits the imaging depth.[56] The NIR optical window near 1700 nm (window III) in the SWIR range can provide deep tissue penetration when both scattering and absorption are considered.[57] Several devices that operate at approximately 1300 nm both *in vivo* and *ex vivo* have been studied.[1,2,58] Both optical coherence tomography (OCT) using a SC light source[4] and three-photon microscopy[57] at 1700 nm are currently used to study structures noninvasively in a living mouse brain. However, the primary characteristics of long-wavelength OCT for deep imaging in biological soft tissue have not been sufficiently studied. In this section, we measured the spectral properties of different biological tissues in the SWIR range using a specific experimental setup,[39] and compared those results with the literature.

1.6.1 Theory

The transmittance of different tissues was measured using a single-mode fiber collimator based on a GRIN lens, as described in Section 1.4. The acceptance

Chapter 2
Luminescence Nanothermometry and Photothermal Conversion Efficiency for Particles Operating in the SWIR Region

Albenc Nexha, Joan Josep Carvajal, and Maria Cinta Pujol
Universitat Rovira i Virgili, Tarragona, Spain

2.1 Light–Matter Interactions

The study of the interactions of light with matter continues to be a major area of research, particularly on the nanoscale. When light illuminates a nanoparticle (NP), different optical phenomena can occur, ranging from luminescence to heat. Luminescence arises from radiative processes, while heat can be generated by nonradiative processes (which can take place within the structure after being excited by light; Fig. 2.1). When the luminescence of a material is temperature dependent, the material can act as a luminescent thermometer.[1,2] If the heat generated by a material falls within the hyperthermia region (from 314 K to 321 K),[3] then the material can be used as a photothermal agent to treat cancer and other diseases.[3,4] Luminescent nanothermometers can provide the temperature at the intratumor or intracellular level,[5,6] detect tumors at early stages,[7] monitor brain activity,[8]

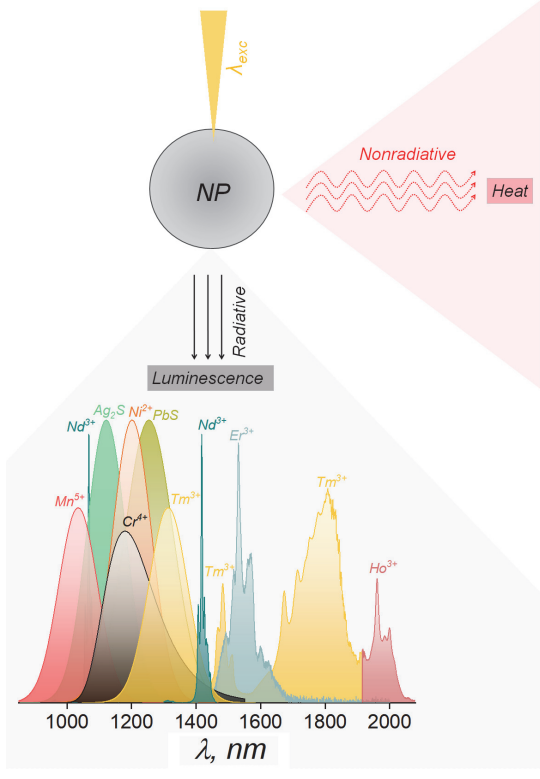

Figure 2.1 Nanoparticle (NP) illuminated by light. Radiative processes lead to luminescence, and nonradiative processes lead to heat. Typical luminescence materials—including quantum dots (QDs: PbS, Ag_2S), transition metals (TMs: Ni^{2+}, Mn^{5+}, and Cr^{4+}), and lanthanide-doped (Nd^{3+}, Er^{3+}, Tm^{3+}, and Ho^{3+}) materials operating in the SWIR region—are shown together with their corresponding wavelength ranges of operation.

2.3 Photothermal Conversion Agents

A particle can absorb light upon illumination. The absorbed light can be converted into luminescence, which can be further used for temperature sensing if the generated luminescence displays temperature-dependent properties as described previously. The absorbed light could also be converted into heat (Fig. 2.1). One way to measure the ability of a material to convert absorbed light into heat is through the photothermal conversion efficiency η. Materials that display this property can be used in photothermal therapy.[3] This process is crucial in preventing and treating cancer and other diseases through control of the heat generated by the particles of the material. In a temperature interval from 314 to 321 K, the heat generated can induce protein aggregation, long-term cell inactivation, and cell death.[3]

Several methods can be used to determine the photothermal conversion efficiency of a material.[3,20] Examples of these methods include: thermal relaxation, based on a study of the kinetics of heating and cooling after switching the excitation source on (heating) and off (cooling);[60] and the integrating sphere method, based on determining the power of the light reflected, transmitted, scattered, and generated by a sample after irradiation with a suitable laser source in an integrating sphere.[61] These two methods are used to determine η for different materials operating as photothermal agents and luminescent thermometers in the SWIR.

Among the types of luminescent materials operating in the SWIR region, only QDs and Ln^{3+}-doped materials have been tested as photothermal agents. For a full overview of photothermal agents—including largely those absorbing light in the VIS and NIR spectral regions—the reader is referred to other references.[3,4,20] To date, to the best of our knowledge, no report has explored the applicability of TM luminescent materials as photothermal agents, probably because these materials are typically excited with UV or VIS light sources. Nevertheless, as the ability of a material to generate heat is attributable to nonradiative processes occurring among their electronic states (excluding plasmonic particles), TMs should in theory exhibit this property; even more so if the TMs are combined with Ln^{3+} ions.

Before discussing QDs and Ln^{3+}-based photothermal agents, it is essential to emphasize that a proper comparison between these types of agents could not be done, as several parameters reported for these two different types of materials are different. Hence, the excitation wavelength, power density, area of illumination, concentration of the particles, and type of method for determination of η greatly influence the η values reported.[3] Furthermore, for these materials, often only a temperature increase of the medium in which they are used has been reported, without specifying the actual value of η (for example, in $Ag@Ag_2S$ QDs[30] or PbS@CdS@ZnS combined with Nd^{3+} ions in a hybrid structure).[26] Therefore, to have a comparison of their performances, we have extracted from the literature the reported η values and

Chapter 3
SWIR Properties of Rare-Earth-Doped Nanoparticles for Biomedical Applications

Yang Sheng
Changzhou University, Changzhou, China

Zhenghuan Zhao
Chongqing Medical University, Chongqing, China

Mei Chee Tan
Singapore University of Technology and Design, Singapore

3.2 Design and Synthesis of REDNs

In general, the host–dopant coupling is tailored to synthesize brightly emitting REDNs. Oxide and fluoride materials are frequently used as hosts due to their high optical transparency in the visible to NIR range and low phonon vibration energy. The rare-earth or lanthanide dopants, which usually form trivalent cations (Ln^{3+}), are generally selected based on their desirable excitation and emission wavelengths. Extensive studies on Ln^{3+} have shown that the single-dopant system generally exhibits relatively poor luminescence efficiency due in part to low absorption cross sections and low-concentration quenching thresholds. Therefore, the majority of REDNs studied today are based on a co-dopant scheme, where one dopant acts as a sensitizer and the other acts as a luminescence emitter, known as an activator. The sensitizer absorbs photon energy from the excitation source and then transfers the energy to the activator, resulting in radiative PL as well as heat due to nonradiative relaxation processes (Fig. 3.2). The energy transfer mechanism is introduced in Section 3.3.

3.2.1 Materials selection for host and dopants

Selection of the host material is critical to the synthesis of REDNs with desirable PL properties. In general, besides transparency in the UV to NIR range (~400–2000 nm), the host material should have a low lattice phonon energy and small lattice mismatch to the dopants. Low lattice phonon energy is essential to minimizing nonradiative energy loss and maximizing the radiative emission. A small lattice mismatch reduces crystal defects such as vacancies and interstitial ions.[12] To date, the most successful host materials are oxide and fluoride materials such as Y_2O_3, $NaYF_4$, and CaF_2.

The host materials themselves do not exhibit PL emission. Therefore, Ln^{3+} is doped into the host materials as localized emitting centers. Er^{3+}, Tm^{3+}, and Ho^{3+} are the most frequently used activators since their

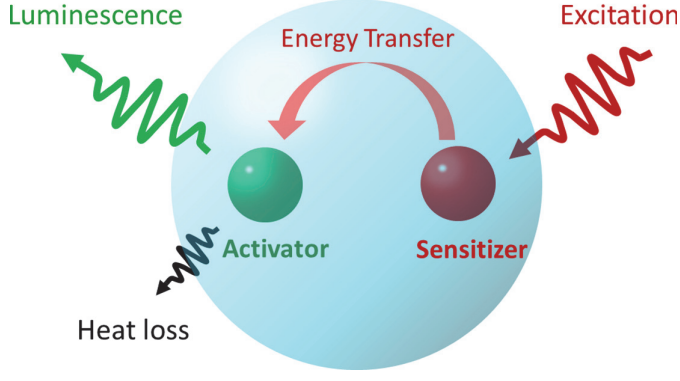

Figure 3.2 Illustration of the PL process of a co-dopant REDN system.

leads to undesired heat as well as reduced penetration depths, which limits the practical application of REDNs for safe and high-resolution *in vivo* imaging. An effective approach to address this issue is to shift the excitation wavelength from 975 nm to either 745 or 800 nm, through use of other rare-earth ions (e.g., Nd^{3+}). By shifting the excitation wavelength, the length of the penetration depth is extended, and the heating effects are reduced significantly. Liang et al. designed core/shell $NaYF_4$:Nd,Yb/$NaYF_4$:Yb,Tm nanoparticles, which achieved 803-nm emission under 745-nm excitation by efficient energy transfer through the $Nd^{3+} \rightarrow Yb^{3+} \rightarrow Yb^{3+} \rightarrow Tm^{3+}$ pathway.[66] This study demonstrates that tissue exposed to 980-nm laser irradiation suffers more than five-fold heating in comparison with tissue irradiated at 745 nm while experimental conditions were maintained the same. The *in vitro* cell viability assay also suggests the significant drawback of the overheating issue, where the hyperthermia produced by 975-nm excitation reduced the cell viability even at low exposure durations, whereas the 745-nm excitation showed no obvious effect on the cell viability.

3.4 Photoacoustic Imaging

Photoacoustic imaging (PAI) has attracted immense attention for high-resolution and deep-tissue visualization, especially for diagnosis of tumor pathophysiological status, minimally invasive characteristics, rapid operation, and accurate quantification.[67,68] In general, PAI is a hybrid imaging modality that combines both optics and ultrasound—providing high ultrasonic spatial resolution (up to several centimeters of penetration depth) and intrinsic optical absorption contrast.[69,70] When a target such as a biological sample is irradiated by a short-pulsed laser beam, which can be either in the visible or SWIR range, a portion of the light is absorbed by the target's constituents and then partially converted into heat, which generates a pressure increase through thermo-elastic expansion.[71] This initial pressure increase, determined by the local optical energy deposition and other thermal and mechanical properties of the target, propagates as an acoustic wave in the biological tissue.[72] When the acoustic wave is detected by highly sensitive ultrasound receivers, the distribution of signal in the sample can be reconstructed.[73]

It is well-established that hemoglobin and melanin are among the most important naturally occurring contrast agents for enhancing PAI contrast.[74] However, the limitations of these intrinsic contrast agents have driven the development of exogenous contrast agents. For example, these intrinsic contrast agents absorb light in the visible spectral region where strong absorption and scattering events occurs, leading to shallow penetration depths. In addition, some diseased sites show a low PA signal due to the low intrinsic optical response of the local tissue chromophore (e.g., lymphatic system).[75]

Polyethylene glycol (PEG)-modified Fe_3O_4@β-$NaGdF_4$:Yb/Er and Yb/Tm were successfully synthesized by Chen et al.[119] They found that the obtained nanostructure still displayed bright PL emissions in the absence of a silica or polymer spacer layer. Furthermore, the coating on the surface of the IONPs did not affect their T_2 contrast ability where a high T_2 relaxivity with the value of 204 $mM^{-1}s^{-1}$ was measured.

Apart from IONPs, dysprosium was also studied to synthesize PL/T_2 dual-mode contrast agents due to its high magnetic moment (10.6 μB) and short electron relaxation time. Yuan et al. synthesized $NaLuF_4$:Yb,Tm/$NaLuF_4$/$NaDyF_4$ nanocrystals with enhanced UCL and MRI signals.[120] A 116-fold enhancement of the emission intensity was observed by coating the layer of $NaDyF_4$ with a measured effective r_2 value of 40 $mM^{-1}s^{-1}$. Due to the excellent optical and T_2 contrast properties, orthotopic pancreatic cancer lesions were detected using these multimodal $NaLuF_4$:Yb,Tm/$NaLuF_4$/$NaDyF_4$ nanocrystals.

3.5.1.4.3 PL/T_1/T_2 triple modalities

Since Gd and Dy can enhance MRI signals by decreasing the relaxation time of a nearby proton in the T_1 or T_2 modes, doping REDNs with both Gd and Dy could potentially create tri-modal PL/T_1/T_2 contrast agents. Zhang et al. synthesized $NaDyF_4$:Yb/$NaGdF_4$:Yb,Er nanoparticles that circumvented the upconverting poisoning effect of Dy^{3+} ions and generated efficient UCL (Fig. 3.13).[121] In addition, the $NaDyF_4$:Yb/$NaGdF_4$:Yb,Er nanoparticles offered not only significant dark T_2-weighted MRI contrast but also bright T_1-weighted MRI contrast properties arising from Dy^{3+} and Gd^{3+}. However, the T_1 contrast ability of this nanosystem was relatively low at 0.32 $mM^{-1}s^{-1}$, limiting its further application as a T_1 contrast agent. The effects of coupling Mn^{2+} to the surface of $NaDyF_4$ nanoparticles on the optical, T_1, and T_2 imaging properties were investigated.[122] Whereas a Mn-complex-modified $NaDyF_4$:Yb@$NaLuF_4$:Yb,Er@polydopamine core/shell nanocomposite exhibited a narrow intrinsic emission band and characteristic UCL emissions, this structure exhibited high T_1 and T_2 contrast ability with values of 4.97 and 277.63 $mM^{-1}s^{-1}$, respectively, which enabled tumor detection in both the T_1 and T_2 modes.

3.5.2 REDN-based theranostic platforms

Investigations on rationally designed REDN-based theranostic platforms have been extensively performed. In the early stages of such research, REDN-based theranostic platforms were used as simple nanocarriers with PL contrast ability to monitor and subsequently overcome the limitation of chemotherapy (e.g., drug dependence, drug resistivity, and poor targeting efficiency). Recently, the unique features of REDNs, including the UC properties and ionizing radiation absorption, have been considered key to address the

Chapter 4
Short-Wave Infrared Meso-Patterned Imaging for Quantitative and Label-Free Tissue Characterization

Yanyu Zhao
Beihang University, Beijing, China

Anahita Pilvar
Boston University, Boston, USA

Mark C. Pierce
Rutgers, The State University of New Jersey, Piscataway, USA

Darren Roblyer
Boston University, Boston, USA

4.1 Introduction to SWIR-Meso-Patterned Imaging

The absorption coefficient μ_a and reduced scattering coefficient μ_s' describe the magnitude of optical absorption and scattering, respectively, in turbid media such as tissue, and can serve as important physiological biomarkers.[1,2]

crossed polarizers to ensure measurement of diffuse light. Images acquired at the three AC illumination phases are demodulated to obtain the tissue response at the corresponding spatial frequency. The demodulation is conducted following Eq. (4.1), which computes the pixel-by-pixel modulation depth (amplitude) at the illuminating AC frequency:

$$I = \frac{\sqrt{2}}{3}\sqrt{(I_1 - I_2)^2 + (I_2 - I_3)^2 + (I_3 - I_1)^2}, \tag{4.1}$$

where I_1, I_2, and I_3 represent raw images corresponding to the three projection phases.

The demodulated images of the tissue are then calibrated against their counterparts from a phantom with known diffuse reflectance to produce diffuse reflectance maps of the tissue under DC and AC illumination. With diffuse reflectance measurements at a minimum of two spatial frequencies, one can calculate μ_a and μ_s' values at each pixel through an analytical or Monte Carlo-based inverse model.[5,7]

After measuring μ_a at multiple wavelengths, the concentration of tissue chromophores such as oxy- and deoxyhemoglobins can be extracted using Beer's law, shown in matrix form in Eq. (4.2), where ε and c refer to the chromophore extinction coefficient and chromophore concentration, respectively:

$$\begin{bmatrix} \mu_a(\lambda_1) \\ \vdots \\ \mu_a(\lambda_j) \end{bmatrix} = \begin{bmatrix} \varepsilon_1(\lambda_1) & \cdots & \varepsilon_i(\lambda_1) \\ \vdots & \ddots & \vdots \\ \varepsilon_1(\lambda_j) & \cdots & \varepsilon_i(\lambda_j) \end{bmatrix} \begin{bmatrix} c_1 \\ \vdots \\ c_i \end{bmatrix}. \tag{4.2}$$

The ε values of chromophores (such as oxy- and deoxyhemoglobin, water, and lipids) are available in the literature.[8,9] Equation (4.2) can be solved for unknown tissue chromophore concentrations c_1, c_2,..., c_i using matrix inversion or regression methods, provided measurements of μ_a have been obtained at $j \geq i$ independent wavelengths.

4.2 The Unique Capabilities of SWIR Light for Quantifying Water and Lipid Content in Tissue

Almost all prior SFDI work utilizes VIS- to NIR-wavelength bands, often between 640 and 850 nm,[10] where the absorption peaks of oxy- and deoxyhemoglobins are prominent. These bands and the absorption spectra of the major tissue chromophores in the visible, NIR, and SWIR wavelength regions—based on typical concentrations found in premenopausal breast tissue—are shown in Fig. 4.1.[17] Oxy- and deoxyhemoglobins are important physiological parameters that can be used to track tissue oxidative

4.5 Examples of Potential Biomedical Applications for SWIR-MPI

SWIR-MPI has multiple potential applications in both preclinical and clinical settings. We briefly introduce several examples, including inflammation monitoring, tumor lipid mapping, brown fat classification, and *in vivo* blood lipid characterization. The experimental conditions and full analyses are presented in Zhao et al.[13]

First, SWIR-MPI was used for longitudinal tracking of edema, which is often associated with inflammation. As an experimental demonstration, 10 μL of phosphate-buffered saline (PBS) or 10 μL of proinflammatory 12-O-tetradecanoylphorbol 13-acetate (TPA) was injected subcutaneously into the flank of BALB/c mice. SWIR-MPI was used to track the local water content for 2 hours post-injection. The measured changes in water content 2 hours after injection are shown in Fig. 4.7(a), demonstrating a significant

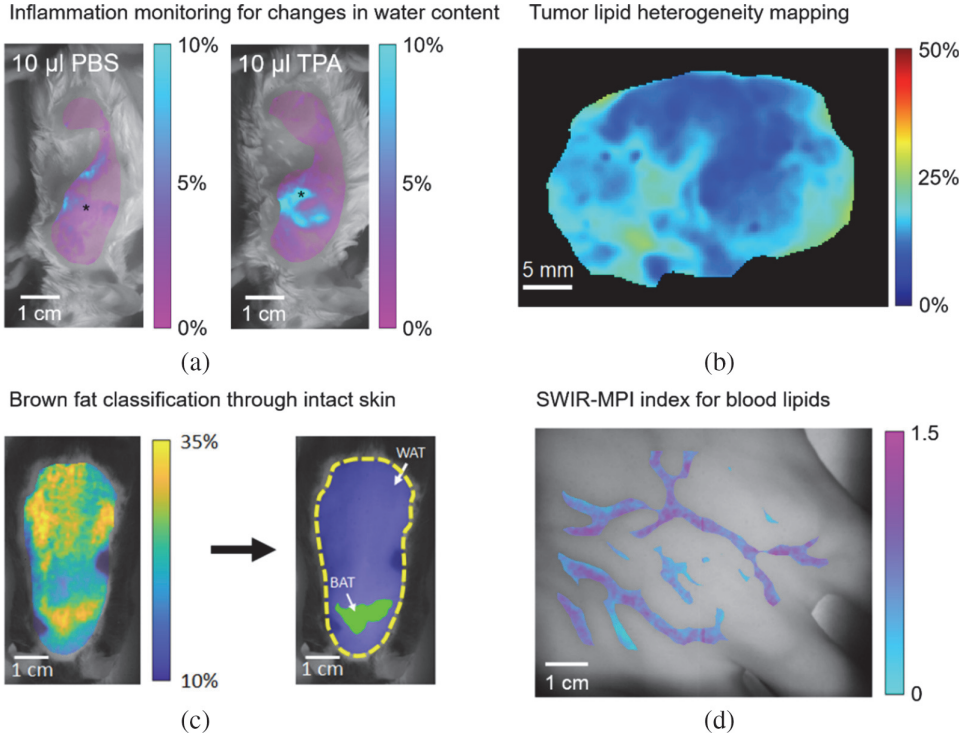

Figure 4.7 (a) Changes of water content induced by inflammation in an *in vivo* mouse model. (b) Lipid content mapping within a tumor cross section. (c) Subcutaneous brown fat classification through intact skin (BAT: brown adipose tissue; WAT: white adipose tissue). (d) SWIR-MPI-based index for blood lipids, measured on the back of the hand in a human subject.

Chapter 5
Short-Wavelength Infrared Hyperspectral Imaging for Biomedical Applications

Lise Lyngsnes Randeberg
Norwegian University of Science and Technology (NTNU), Trondheim, Norway

Julio Hernández
HySpex, Norsk Elektro Optikk AS, Oslo, Norway

Emilio Catelli
University of Bologna, Ravenna Campus, Italy and Norwegian University of Science and Technology (NTNU), Trondheim, Norway

genitourinary systems." However, despite their extensive review, Ortega et al.[5] and Gao and Smith[9] list few papers on SWIR, leaving SWIR as a relativity unexplored area of HSI and an area for future efforts.

Gowen et al.[19] review applications of HSI in microbiology and cover several applications in the SWIR range, but the applications are mainly related to food science. However, applications such as detection of fungi on surfaces and pathogenic bacteria (such as *Staphylococcus epidermidis* and *Enterobacteria* in water, and biofilms from *Escherichia coli* on microfluidic cells) are highly relevant for biomedical applications.[101–105] In general, food sciences have provided a large number of relevant studies on characterization and detection of bacteria that could be adapted to a medical context.

Skin—the most accessible organ on the human body and one of the largest organs—is the organ most explored by HSI, including characterization of healthy tissue and conditions of pathologies affecting the skin. Initial studies include examples on circulatory changes and skin oxygenation in diabetic feet.[93] Allergic contact dermatitis, burns, and ulcers are more recent examples of HSI of skin[75,93,94] (Fig. 5.5). Randeberg[75] presents hyperspectral data in the SWIR range, discusses spectral characteristics of spectra from a burn model, and shows that unsupervised classification methods such as *k*-means could be applied for burn classification.

In the field of forensics, HSI has been used to investigate crime scenes, to identify stains of biological fluids and blood on soft materials such as clothing, and for characterizing skin bruises.[73,74,106–108] Bruises are caused by ruptured blood vessels and leakage of blood into the tissue. Immediately after the trauma, there will be a wheal and flare reaction, which is characterized by swelling and fluid accumulation.[109] It has been shown that, in the SWIR spectral range, it is possible to differentiate between blood and other fluids accumulating in the injured area[74] (Figs. 5.6 and 5.7 show the spectra from bruised skin in subjects with skin types II and IV). These spectra clearly show that the influence from pigmentation is limited in the SWIR spectral range. Paintballs induce circular bruises with an undamaged central spot, due to central compression of the skin directly underneath the paintball, and the shear force at the edge of the paintball causes vessel rupture. When imaging a fresh paintball bruise in the SWIR, the central area will appear swollen, while a rapidly developing hemorrhage can be seen at the edges.

5.3 Hyperspectral Instrumentation and Setup

HSI was initially developed for remote sensing and satellite imaging. In 2005, Sellar and Boreman classified imaging spectrometers for HSI[34] and defined a taxonomy for imaging spectrometers. According to Boreman's definitions, and highlighted in an overview provided by Wu and Sun,[13] hyperspectral instrumentation and data collection is divided into four types. The first type is

cross-validation (CV) temporarily removes part of the data to simulate an independent test set.[166]

With either a new validation test set or an independent validation test set, we can evaluate the results of the calibration model using two equations: the root mean-square error (RMSE) equation and the R^2 coefficient, both of which are terms for the calibration, cross-validation, and predictive ability. Low values of the RMSE with an R^2 coefficient close to 1 indicate good performances of the model in terms of predictive ability:

$$RMSE = \sqrt{\frac{\sum_{i=1}^{n} (y_i - \hat{y}_i)^2}{n}} \tag{5.9}$$

$$R^2 = 1 - \frac{\sum_{i=1}^{n} (y_i - \hat{y}_i)^2}{\sum_{i=1}^{n} (y_i - \bar{y}_i)^2}, \tag{5.10}$$

where y and $\bar{y}$ (mean) are experimental, $\hat{y}$ is the predicted value for sample i, and n is the total number of samples.

5.8 Machine Learning and Artificial Intelligence

It is no doubt that machine learning [a form of artificial intelligence (AI)] and especially deep learning can greatly enhance HSI. By using appropriate auto-encoders, the algorithms can work on data without dimensionality reduction, noise removal, or separate feature extraction. However, there are disadvantages. In 2018, a workshop was held to develop a roadmap for foundational research on AI in medical imaging.[167] Researchers highlighted several state-of-the-art applications of AI in medicine, which are as follows:

1. New image reconstruction methods that efficiently produce images suitable for human interpretation from source data.
2. Automated image labeling and annotation methods—including information extraction from the imaging report, electronic phenotyping, and prospective structured image reporting.
3. New machine-learning methods for clinical imaging data—such as tailored, pretrained model architectures, and federated machine learning methods.
4. Machine-learning methods that can explain the advice they provide to human users (i.e., explainable AI).

Chapter 6
VIS–SWIR Wideband Lens-Free Microscopic Imaging

Ziduo Lin, Abdulkadir Yurt, Geert Vanmeerbeeck, Murali Jayapala, Zhenxiang Luo, Jiwon Lee, Joo Hyoung Kim, Vladimir Pejovic, Epimitheas Georgitzikis, Pawel Malinowski, and Andy Lambrechts
Imec—Interuniversity Microelectronics Center, Leuven, Belgium

6.1 Introduction

Microscopes are an integral part of most biomedical research. Over the last several years, microscopy has been utilized with wavelengths of light beyond the visible spectrum in the short-wavelength infrared (SWIR). SWIR microscopy provides several advantages over visible and near-infrared (NIR) microscopy, including lack of (or minimal) autofluorescence, low light absorption by blood and tissues, and reduced scattering. However, extending the spectral range of microscopic instruments from the visible to the SWIR is challenging because of optical equipment such as sensors and other components. Digital image sensors typically provide good sensitivity but only in a limited spectral range. They can be used for imaging in the visible or

Chapter 7
SWIR Fluorescence and Monte Carlo Modeling of Tissues for Medical Applications

Tatsuto Iida, Shunsuke Kiya, and Kosuke Kubota
Maebashi Institute of Technology, Maebashi, Japan

Akitoshi Seiyama
Kyoto University, Kyoto, Japan

Takashi Jin
RIKEN Center for Biosystems Dynamics Research, Suita, Japan and Osaka University, Osaka, Japan

Yasutomo Nomura
Maebashi Institute of Technology, Maebashi, Japan and RIKEN Center for Biosystems Dynamics Research, Suita, Japan

restricted by absorption and scattering, and the absorption and scattering coefficients at 488 nm are larger than those at 780 nm (Table 7.2). Notably, almost no fluence is observed at 488 nm at a depth less than 1.0 cm, even though a fluorophore-labeled cancer with a diameter of 1.0 cm is localized in a deeper area of the circle, which is indicated by dotted lines [Fig. 7.9(a)]. Therefore, no fluorophores within the cancer are excited and no emission photons are observed [Fig. 7.9(b)].

In contrast, NIR excitation photons at 780 nm extensively propagate in the model, and the weights are partially absorbed [Fig. 7.9(c)]. Compared with the region near the origin where excitation photons enter, fluence in the cancer is weak and the difference in fluence among grids within the cancer is also minor. Therefore, as a first step to establish the breast cancer model, it may be appropriate to generate emission photons with a constant weight at a randomly determined position, but generation of emission photons with an initial weight that is dependent on the position is necessary in subsequent steps, as described in the next section. As illustrated in Fig. 7.9(d), each photon that emits from the fluorophore-labeled cancer propagates isotropically.

SWIR-excitation photons migrate the widest and deepest among the three types of excitation photons, and the grid area of the cancer has the highest fluence [Fig. 7.9(e)]. SWIR-emission photons migrate more widely and deeper than NIR-emission photons [Fig. 7.9(f)]. In order to simplify the calculation, the heterogeneity due to the finite cancer volume is ignored, although there may be an excitation gradient within a cancer having a finite volume. This is an important problem to be solved and is discussed in the next section.

7.4 SWIR Fluorescence Model in Voxelized Media (MCVM) for Breast Cancer

In the final section of this chapter, a fluorescence-labeled cancer is embedded into the model reflecting a realistic breast structure. In the previous section, the breast tissue is assumed to have a multilayered structure made of skin and fat. However, in addition to the two components of the tissue, breast tissue contains mammary glands with a complex morphology, which is made of ducts and lobes. Breast cancer patients usually develop breast cancer in the duct. To develop a realistic breast cancer model, an anatomical dataset of the breast is implemented in the Monte Carlo model.[58] In the previous section, fluorophores within the spherical cancer receive a constant energy fluence from the excitation photons. Here, fluorophores are excited in a manner that depends on the excitation energy fluence of each voxel within the cancer. Using MCVM, which is more realistic than MCML, the significance of SWIR fluorescence imaging of breast cancer is discussed.

Chapter 8
Multimodal SWIR Laser Imaging for Assessment and Detection of Urothelial Carcinomas

Gustavo Castro-Olvera
ICFO, The Barcelona Institute of Science and Technology, Castelldefels, Spain

Simone Morselli, Mauro Gacci, Sergio Serni, Andrea Liaci, and Rosella Nicoletti
University of Florence, Florence, Italy

Pablo Loza-Alvarez
ICFO, The Barcelona Institute of Science and Technology, Castelldefels, Spain

Chapter 9
SWIR Fluorescence Endoscopy for Tumor Imaging

Yongkuan Suo and Hongguang Liu
Northeastern University, Shenyang, China

Zhen Cheng
Stanford University, Stanford, United States

9.1 Introduction

Interventional therapy, supported by medical imaging (angiography, computed tomography, magnetic resonance, or endoscopy), uses the natural lumen of the human body to treat a blood vessel or lesioned part of the body. Interventional therapy has the advantages of minimal trauma, few complications, quick curative effects, strong reproducibility, and short recovery time for patients. In addition, interventional therapy has been widely used in medical treatments of vascular thrombolysis, in vascular stents, and for diseases of internal organs—such as the lungs, esophagus, stomach, and intestines—and of the abdominal cavity.

For the treatment to be done correctly, the process of interventional therapy needs to be guided and monitored by an imaging device in order to precisely reach the lesion. For example, coronary angiography, thrombolysis, and stent implantation in the treatment of angina pectoris and acute myocardial infarction are typical vascular interventional therapy technology applications. However, because of the poor opacity of blood and the complexity of the vascular network through various tissues, the images are usually obtained by radiological imaging

Chapter 10
Short-Wavelength Infrared Hyperspectral Imaging to Assess Gastrointestinal Stromal Tumors During Surgery

Toshihiro Takamatsu
Tokyo University of Science, Noda, Japan and National Cancer Center, Kashiwa, Japan

Hiroaki Ikematsu
National Cancer Center, Kashiwa, Japan and National Cancer Center Hospital East, Kashiwa, Japan

Hiroshi Takemura
Tokyo University of Science, Noda, Japan

Hideo Yokota
RIKEN Center for Advanced Photonics, Wako, Japan

Kohei Soga
Tokyo University of Science, Noda, Japan

Chapter 12
Transparent Polycrystalline Ceramic Cranial Implant with Photonic Functionality in the SWIR

Santiago Camacho-López
Centro de Investigación Científica y de Educación Superior de Ensenada, Ensenada, Mexico

Nami Davoodzadeh and David L. Halaney
University of California, Riverside, United States

Juan A. Hernández-Cordero
Universidad Nacional Autónoma de México, Ciudad de México, Mexico

Guillermo Aguilar
University of California, Riverside, United States and Texas A&M University, College Station, United States

Gabriel R. Castillo
Centro de Investigación Científica y de Educación Superior de Ensenada, Ensenada, Mexico; and Universidad Nacional Autónoma de México, Ensenada, Mexico

Antonio Cisneros-Martínez and Beatriz Coyotl-Ocelotl
Instituto Nacional de Astrofísica, Óptica, y Electrónica, Tonantzintla, México

Roger Chiu
Universidad de Guadalajara, Lagos de Moreno Jalisco, México

Julio C. Ramírez-San-Juan and Rubén Ramos-García
Instituto Nacional de Astrofísica, Óptica, y Electrónica, Tonantzintla, México

Camacho-López are working on different strategies to efficiently couple optical fibers in and out of the waveguides, to make it possible to bring light from an external source into the brain tissue, for the purpose of diagnostics and/or therapeutic treatment of specific brain lesions. We have also considered the possibility of drug photoactivation under appropriate light exposure, aimed at localized tissue that is the target of the drug provided through systemic delivery.

Researchers broadly recognize nc-YSZ as one of the most useful high-temperature structural materials due to its favorable ionic conducting properties,[58] high-temperature stability,[59] record toughness,[46] and proven biocompatibility.[26] While these properties make nc-YSZ a promising material for extreme integrated photonic applications, this material has been largely overlooked. This is because YSZ is not generally considered an optical material, owing to the poor/extant optical quality of conventionally produced YSZ polycrystals. However, thanks to work by Garay et al.[46] on the CAPAD technique, nc-YSZ is now produced in optical grade. Thus, a multidisciplinary effort has been made to integrate the WttB platform based on the nc-YSZ ceramic.

We can summarize our findings by highlighting the fact that we demonstrated the feasibility of femtosecond laser writing of waveguides in polycrystalline nc-YSZ. Prior to our work, direct laser writing (DLW) of photonic structures in ceramics was largely untested. This is because today there are only a limited number of groups worldwide that can produce optical-grade NC ceramics. This DLW in ceramics technique represents a new direction for integrated photonics. Moreover, NC ceramics offer high temperature/chemical stability, superior mechanical toughness, and greater fabrication flexibility when compared to glasses and single crystals.

12.4 Imaging through Highly Scattering Media

Propagation of light in biological tissues is a popular research topic since light can provide useful information for diagnosis and treatment of many medical conditions; in particular, traumatic brain injury and brain disorders (such as Alzheimer's disease, dementias, brain cancer, epilepsy, mental disorders, Parkinson's, stroke, and transient ischemic attack) are the most-difficult-to-treat medical conditions, given the difficulty of accessing the brain. For such reasons, light-based techniques are promising medical options. However, light penetration is hindered by light absorption and scattering from the tissue and skull. Fortunately, tissue and bones are more translucent—allowing light to penetrate deeper—but are also heterogeneous, resulting in distorted wave-fronts and light scattering in many directions. Visualization of blood vessels is critical to identify abnormalities and measurement of blood flow, but image-bearing light is rapidly attenuated, and the spatial information is lost as

12.5 Optical Fiber Probes for Diagnostics and Therapeutics

It is clear that nc-YSZ provides attractive optical and mechanical features for the WttB platform. In particular, it offers adequate transparency over the SWIR optical regions that allow for implementing procedures for therapeutics and diagnostics with optical techniques. For instance, imaging methods and PDT can be readily performed through this material, and use of OCAs may further extend the versatility of the WttB platform. Some procedures however may still require access to deeper regions of the brain, and it is for these purposes that we have been exploring novel approaches for developing optical fiber probes. In particular, we have focused on fabrication of sensors and devices that could serve either as auxiliary tools for therapeutic and diagnostic procedures, or as building blocks for fiber-optic probes—enabling thermal-based therapeutics such as ablation and hyperthermia. These are of interest for treating cancerous tissue and, combined with other established therapeutic techniques (e.g., chemotherapy or radiotherapy), have yielded promising results for reduction or elimination of brain tumors.

Our approach for fabricating fiber devices is based on combining silica-based fibers with polymeric materials of different functionalities. We have explored, in particular, the use of PDMS—a polymer with remarkable thermal, mechanical, rheological, and biological properties[85,86] that is common and easy to process. Through simple mixing procedures, we have demonstrated that PDMS can serve as a host for different nanomaterials, including carbon-based structures and fluorescent powders.[87,88] This method yields polymer composites that can be easily fabricated and processed to be incorporated into optical fibers, or simply used as membranes with interesting effects that can be triggered by infrared light irradiation.[87] While fluorescent polymer composites are useful for developing sensors for fluorescent thermometry,[88] PDMS composites incorporating carbon nanoparticles (CNPs) serve for generating thermal effects in a highly efficient manner. These PT effects are useful for a wide range of applications (refer to Ref. 87 for some examples) and can be further exploited to fabricate other devices such as fiber-optic sensors. We describe temperature and deformation sensors as well as PT devices that have been developed within the WttB research framework. These devices are sought as building blocks for more-complex devices such as fiber-optic probes for therapeutic procedures.

12.5.1 Fiber-optic temperature sensors

The temperature sensors are based on the fluorescence features of the PDMS composites; these incorporate rare-earth-doped materials that have been previously optimized to generate green upconversion (UC) luminescence.

Chapter 13
SWIR Hyperspectral Imaging to Assess Neurocognitive Disorders Using Blood Plasma Samples

Raquel Leon, Abian Hernandez, and Himar Fabelo
Instituto Universitario de Microelectrónica Aplicada, Universidad de Las Palmas de Gran Canaria, Las Palmas de Gran Canaria, Spain

Samuel Ortega
Instituto Universitario de Microelectrónica Aplicada, Universidad de Las Palmas de Gran Canaria, Las Palmas de Gran Canaria, Spain and Nofima—The Norwegian Institute of Food, Fisheries and Aquaculture Research, Tromsø, Norway

Francisco Balea-Fernández and Gustavo M. Callico
Instituto Universitario de Microelectrónica Aplicada, Universidad de Las Palmas de Gran Canaria, Las Palmas de Gran Canaria, Spain

13.4 Experimental Results and Discussion

In this section, the results obtained using the proposed ML and DL approaches for processing the SWIR blood plasma samples are presented. The section is divided into the presentation of the results obtained using the validation and test sets, and also employing different data normalizations.

13.4.1 Validation classification results

The validation set was employed to optimize the hyperparameters of the ML algorithms as explained in Section 13.3.1. The results obtained after performing a grid search using the ML approach are presented in Table 13.2, where the selected hyperparameters were those that achieved higher AUC values. Furthermore, one can observe in Table 13.2 that the AUC values were obtained applying different data normalizations, where the SVM classifier with a linear kernel (SVM-L) achieved the higher AUC value for each data normalization type. The data normalization has no effect on the AUC results obtained using the RF classifier. In the case of the SVM-L and KNN classifiers, the data normalization deteriorates the AUC results with respect to the use of the data without normalization. These results suggest that data normalization does not necessarily correspond to an improvement in the classification performance. Hence, the best classification model is obtained with the SVM-L without applying data normalization, achieving an AUC of 0.72.

Considering the DL approach based on the MLP classifier described in Section 13.3.2, the results obtained are presented in Table 13.3 with and without applying different data normalizations. Unlike the previous results

Table 13.2 Grid search results using different ML classifiers with and without applying the different data normalizations (where HP refers to hyperparameters).

			Grid search		
Normalization type	**Classifier**	**HP**	**Initial/step/final**	**Optimal HP**	**AUC**
None	SVM-L	C	$2^{-20}/2^{2}/2^{20}$	2^{-14}	0.720
	KNN	N_T	1/2/600	17	0.612
	RF	K_{NN}	1/2/600	197	0.625
NOR	SVM-L	C	$2^{-20}/2^{2}/2^{20}$	2^{-8}	0.707
	KNN	N_T	1/2/600	11	0.573
	RF	K_{NN}	1/2/600	197	0.625
SOR	SVM-L	C	$2^{-20}/2^{2}/2^{20}$	2^{-8}	0.706
	KNN	N_T	1/2/600	7	0.573
	RF	K_{NN}	1/2/600	197	0.625
BOR	SVM-L	C	$2^{-20}/2^{2}/2^{20}$	2^{-8}	0.707
	KNN	N_T	1/2/600	7	0.572
	RF	K_{NN}	1/2/600	55	0.625

Chapter 15
Use of a SWIR Otoscope in the Assessment of Pediatric and Other Conditions

Nirvikalpa Natarajan, Yu-Jin Lee, and Tulio A. Valdez
Stanford University, Stanford, United States

15.1 Introduction

Otitis media (*ot*-ear, *itis*-inflammation, *media*-middle ear) is one of the most common illnesses diagnosed in children. Globally, with an incidence of over 709 million,[1–3] it is the most common reason for administering antibiotics to

Chapter 16
Use of an OCT System in the Short-Wavelength Infrared Region: Applications

Pauline John
Sri Sivasubramaniya Nadar (SSN) College of Engineering, Kalavakkam, India

Vani Damodaran
SRM Institute of Science and Technology, Kattankulattur, India

Nilesh J. Vasa
Indian Institute of Technology Madras (IITM), India

Chapter 18
Advances in SWIR Deep Tissue Imaging Using Machine Learning

Laura A. Sordillo
Allosteric Bioscience, Inc., New York, United States

Diana C. Sordillo
Vanderbilt University, Nashville, United States

18.1 Introduction

Recently, machine learning (ML), a form of artificial intelligence (AI), has emerged as an important technique in biophotonics, an interdisciplinary field of science that merges the studies of light (photons) and medicine. Applications of ML algorithms to medicine include data preprocessing, feature detection, drug discovery, and disease classification, among others.[1] In fact, it has been suggested that the use of ML algorithms, in particular deep learning (DL), may revolutionize biophotonics.

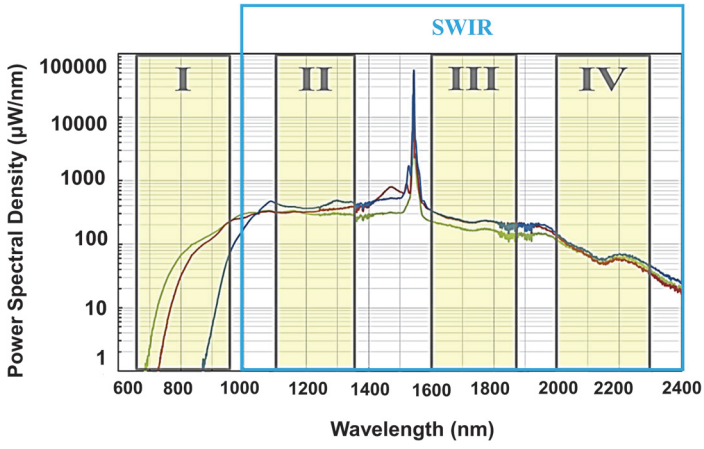

Figure 18.3 Pump spectrum from the Leukos SC laser light source, with windows I, II, III, and IV highlighted.

the SWIR range at ~1200 and ~1700 nm, corresponding to NIR windows II and III, respectively.

The Leukos SC laser operates with a 1550-nm pump and delivers 40-ps pulses at 6 MHz. Figure 18.3 shows the power spectrum of the SC laser light source with a maximum power of ~500 μW/nm in the SWIR range.

When compared with a conventional broadband lamp light source, the SC laser light source, which provides a greater number of outgoing photons, was able to reach a greater depth of penetration and give higher-quality images of abnormalities hidden behind thick tissue. While SWIR light can provide major benefits, such as an increase in penetration depth and a reduction of absorption and scattering of light, acquisition of high-quality optical images through thick tissue (even with a powerful SC laser light source) remains a challenge. Thus, there is still a need for additional techniques that can provide efficient assessment and detection as well as high-quality optical images of abnormalities hidden beneath thick tissue. ML techniques may be utilized to enhance these biophotonic techniques.

18.3 Deep Learning Models

18.3.1 Overview of deep learning

Machine learning (ML) is a branch of artificial intelligence (AI) that uses sample data to make predictions about new, previously unseen data.[20,21] Deep learning (DL) is a class of ML algorithms based on artificial neural networks (ANNs). An ANN is a ML algorithm that learns through labeled data (supervised learning) and was originally modeled after the learning process of the human brain. Introduced in 1958 by Rosenblatt, the first ANN was called the perceptron. In the perceptron model, inputs $\mathbf{x} = (x_1, \ldots, x_d)$ are first

probability of x, given y), whereas discriminative models calculate the conditional probability $p(y|x)$ (the probability of y, given x).[31]

In the simplest case of a GAN, both G and D can be taken to be MLPs. Given a training set, G generates new data with the same statistics as the training set. D is trained to maximize the probability of assigning the correct label to both the training samples and the samples generated by G. Simultaneously, G is trained to maximize the error rate of D.[30] GANs can be for image classification, image manipulation and generation, and super-resolution.[32] Shrivastava et al. developed a GAN capable of generating highly realistic images.[33] Thus, GANs can be used to create more training samples when there is limited labeled training data available. Ledig et al. developed SRGAN, a GAN for image super-resolution.[34]

ResNets were introduced by He et al. in 2015, winning first place in the classification task at ILSVRC 2015 by achieving a 3.57% error on the ImageNet test set.[35] In ResNets, instead of hoping the stacked layers fit the desired underlying mapping $\mathcal{H}(\mathbf{x})$, the stacked nonlinear layers fit the mapping $\mathcal{F}(\mathbf{x}) = \mathcal{H}(\mathbf{x}) - \mathbf{x}$. Then, the original mapping can be recast into $\mathcal{F}(\mathbf{x}) + \mathbf{x}$, which can be realized by a feed-forward neural network with skip connections. ResNets can be trained by backpropagation and are considered to be easier to optimize than CNNs and ANNs. They are used in classification tasks and data processing.

In 2015, Ronneberger et al. proposed the U-Net, a modification of a fully connected convolutional network for biomedical image segmentation.[36] Fully convolutional networks (FCNs) were first introduced by Long et al. in 2015.[37] FCNs take the usual contracting CNN architecture and supplement it with successive layers, but the pooling layers are replaced by upsampling operators. This allows for increased resolution of the output.

U-Nets are a modification of the FCN architecture. The U-Net architecture consists of a contracting path and an expansive path. The contracting path has the usual CNN architecture. The expansive path consists of upsampling of feature maps followed by convolution. Only a few training images are needed for U-Nets, which yield a more-precise segmentation than FCNs.[37]

18.4 Machine Learning Techniques, SWIR, and Disease

18.4.1 Machine learning and biophotonics

The intersection of two advanced fields of science—AI (or ML) and biophotonics—has caused an explosion of studies focusing on ways to assess and detect disease better than previously possible.[38–43] ML has been applied to biophotonic techniques, such as fluorescence and Raman spectroscopy, and to optical imaging (Fig. 18.5).